Chinese Journal of
POLYMER SCIENCE

RESEARCH ARTICLE

https://doi.org/10.1007/s10118-026-3655-0
Chinese J. Polym. Sci. **2026**, *44*, 2534–2548

Modulating Molecular Electrostatic Potential Unlocks Efficient Exciton Dissociation in A-D-A-type Narrow Bandgap Acceptors-based Organic Solar Cells

Jin Li[a,†], Ping Jiang[a,†], Hao-Jia Ding[a,†], Ming-Tao Liu[a,†], Yue Zhen[a], Dan Liu[a], Jia-Nan Fang[a], Pei-Pei Zhu[a*], Shen-Bo Zhu[b], Hua-Wei Hu[b], Xun-Fan Liao[a*], and Yi-Wang Chen[a,c*]

[a] *Key Laboratory of Fluorine and Silicon for Energy Materials and Chemistry of Ministry of Education/National Engineering Research Center for Carbohydrate Synthesis, College of Chemistry and Materials, Jiangxi Normal University, Nanchang 330022, China*
[b] *State Key Laboratory of Advanced Fiber Materials & College of Materials Science and Engineering, Donghua University, Shanghai 201620, China*
[c] *College of Chemistry and Materials, Gannan Normal University, Ganzhou 341000, China*

Electronic Supplementary Information

Abstract Multithiophene-based fused-ring electron acceptors (MFREAs) have demonstrated remarkable performance not only in organic solar cells, but also in other optoelectronic devices owing to their extended near-infrared absorption. However, an insufficient electrostatic potential (ESP) difference with the donor results in a weak intermolecular electric field (IEF), which leads to low exciton dissociation efficiency. In addition, the narrow bandgap causes substantial energy loss (E_{loss}), thereby restricting the open-circuit voltage. To address these problems, we developed two novel MFREAs, 6TFIC-C11-4F and 6TFIC-C11-4Cl, which were developed from the typical molecule 6TIC-4F *via* central-core side-chain fluorination and terminal chlorination. Although core fluorination slightly attenuated the intramolecular charge transfer (ICT) effect, this strategy significantly increased the overall average ESP value, strengthening the donor-acceptor IEF, thereby facilitating exciton dissociation. Terminal chlorination enhanced the ICT effect, resulting in a red-shifted absorption spectrum and stronger IEF. Notably, 6TFIC-C11-4F exhibited increased intermolecular interactions and reduced π-π stacking distances, leading to better charge transport. As a result, the PM6:6TFIC-C11-4F device achieved a decent power conversion efficiency of 13.32%, significantly outperforming the PM6:6TIC-4F device (10.52%). In addition, the PM6:6TFIC-C11-4Cl device demonstrated reduced E_{loss} and a higher short-circuit current density, validating the potential of central-core side-chain fluorination and terminal chlorination in designing high-performance MFREAs.

Keywords Multithiophene fused-ring electron acceptors; Organic solar cells; Central-core side-chain fluorination; Electrostatic potential; Exciton dissociation

Citation: Li, J.; Jiang, P.; Ding, H. J.; Liu, M. T.; Zhen, Y.; Liu, D.; Fang, J. N.; Zhu, P. P.; Zhu, S. B.; Hu, H. W.; Liao, X. F.; Chen, Y. W. Modulating molecular electrostatic potential unlocks efficient exciton dissociation in A-D-A-type narrow bandgap acceptors-based organic solar cells. *Chinese J. Polym. Sci.* **2026**, *44*, 2534–2548.

INTRODUCTION

Organic solar cells (OSCs) have emerged as a promising clean-energy technology for achieving carbon neutrality, owing to their light weight, solution processability, and low manufacturing cost.[1–4] During the early stages of OSCs development, fullerenes and their derivatives dominated bulk-heterojunction (BHJ) OSCs.[5–7] However, limitations such as energy-level mismatch with donors and low utilization of near-infrared photons restrict the efficiency of fullerene-based OSCs to approximately 12%.[8–10] In 2015, Lin *et al*. developed the first fused-ring electron acceptor (FREA) ITIC. It has an acceptor-donor-acceptor (A-D-A) structure based on an electron-donating fused aromatic core indacenodithieno[3,2-*b*]thiophene (IDTT) coupled with strong electron-accepting end groups, and thus has advantages such as strong absorption in the visible region and good morphological stability in the blend film.[11] Owing to the expanded conjugated plane of the "D" unit, ITIC significantly enhances π-electron delocalization and the intramolecular charge transfer (ICT) effect, thereby improving device performance. Consequently, ITIC series electron acceptors have received extensive attention from researchers.[12–14] In 2017, Dai *et al*. designed the first multithiophene-based fused-ring electron acceptor (MFREA) IHIC by replacing the benzene ring in the IDTT unit with a thieno[3,2-*b*]thiophene (TT) unit. The IHIC demonstrates strong near-infrared (NIR) absorption with a narrow opti-

* Corresponding authors, E-mail: ppzhu@jxnu.edu.cn (P.P.Z.)
E-mail: xfliao@jxnu.edu.cn (X.F.L.)
E-mail: ywchen@ncu.edu.cn (Y.W.C.)
† These authors contributed equally to this work.
Received December 29, 2025; Accepted March 10, 2026; Published online June 22, 2026

cal bandgap of 1.38 eV.[15]

The "D" unit of MFREAs is constructed through the fusion of multiple thiophene and cyclopentadiene units. Owing to the extended π-electron delocalization pathways of the TT unit compared to the benzene rings, these acceptors exhibit narrower optical bandgaps (1.25–1.40 eV). Combined with their high electron mobility, these materials demonstrate broad applicability in OSCs and other optoelectronic devices.[16–20] For example, as a prototypical molecule in MFREAs, 6TIC-4F (also named F8IC) has been extensively utilized in OSCs and has demonstrated remarkable performance in semi-transparent OSCs (ST-OSCs), organic photodetectors (OPDs), perovskite solar cells (PVSCs), and near-infrared II (NIR-II) phototheranostic agents (PTAs) (Fig. 1).[21–26]

However, the efficiency of OSCs based on this acceptor remains relatively low (<12%), primarily attributed to: (1) energy-level mismatch with high-performance donors such as PM6, leading to low open-circuit voltage (V_{OC}); (2) steric hindrance from bulky side chains on the central core benzene ring, resulting in weak molecular packing; and (3) small molecular surface electrostatic potential (ESP) differences between donor and acceptor, which hinders the strong intermolecular electric field (IEF) and consequently reduces the short-circuit current density (J_{SC}). The literatures suggest that fluorination of the central core benzene ring can improve molecular packing and optimize the crystallographic orientation.[27,28] Also, the incorporation of fluorine atoms enhances the overall electron-deficient character of the acceptors, thereby strengthening the donor-acceptor IEF to promote exciton dissociation efficiency and increase J_{SC}. Simultaneously, fluorination increases the molecular dipole moment, which reduces the exciton binding energy and consequently suppresses non-radiative recombination, thereby lowering the non-radiative energy loss (ΔE_3).[29–31] Additionally, the introduction of alkyl side chains at the β-position of TT units improves acceptor solubility and elevates the lowest unoccupied molecular orbital (LUMO) energy levels, which is beneficial for enhancing V_{OC} in devices.[32–35] Furthermore, terminal chlorination has been shown to enhance the ICT effect while further increasing the electron-deficient character of acceptors, thereby improving J_{SC}.[36–39] Meanwhile, terminal chlorination has been proven to be effective in reducing ΔE_3.[40,41]

In this study, 6TIC-4F, a typical molecule in MFREAs, was selected as a paradigm for material modification owing to its remarkable performance in diverse applications. By introducing an undecyl chain ($-C_{11}H_{23}$) at the β-position of the TT unit and fluorine atoms into the central side chain of the ultra-narrow-bandgap acceptor 6TIC-4F, novel MFREA 6TFIC-C11-4F and its terminal-chlorinated derivative 6TFIC-C11-4Cl were synthesized and applied to OSCs (Fig. 2a). The two acceptors exhibit excellent molecular coplanarity and possess very deep LUMO energy levels. Research shows that although core fluorination slightly attenuates the ICT effect, this strategy significantly increases the overall average ESP value of acceptors, enhances their electron-deficient character, and strengthens the donor-acceptor IEF, thereby facilitating exciton dissociation. In addition, the single crystal data illustrated that 6TFIC-C11-4F exhibited better 3D network stacking, demonstrating better intermolecular interactions, and this result aligns well with the two-dimensional grazing incidence wide-angle X-ray scattering (2D-GIWAXS) data. Terminal chlorination of 6TFIC-C11-4F enhanced the ICT effect and further strengthened the electron-withdrawing ability, resulting in a red-shifted absorption spectrum and a stronger IEF. Both acceptors, together with 6TIC-4F, were subsequently employed in OSCs devices to systematically study the impact of molecular structural changes on the photovoltaic performance. When prepared by blending each of these three acceptors with the energy-level and absorption-matched polymer donor PM6, it was found that the PM6:6TFIC-C11-4F based device exhibited the best PCE of 13.32%, which was attributed to better molecular packing and higher exciton dissociation. The exciton dissociation of the PM6:6TFIC-C11-4F based device was as high as 94.0%, which was much higher than that of the PM6:6TIC-4F based device (86.3%), indicating a larger ESP difference between PM6 and the acceptor, result-

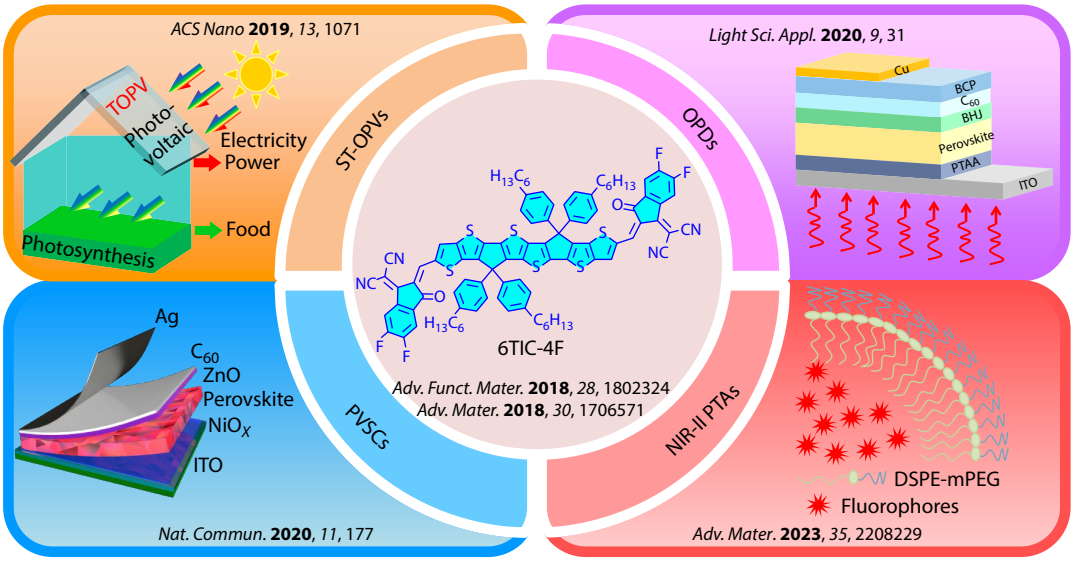

Fig. 1 Widely application of 6TIC-4F or F8IC in ST-OPVs, PVSCs, OPDs and NIR-II PTAs.

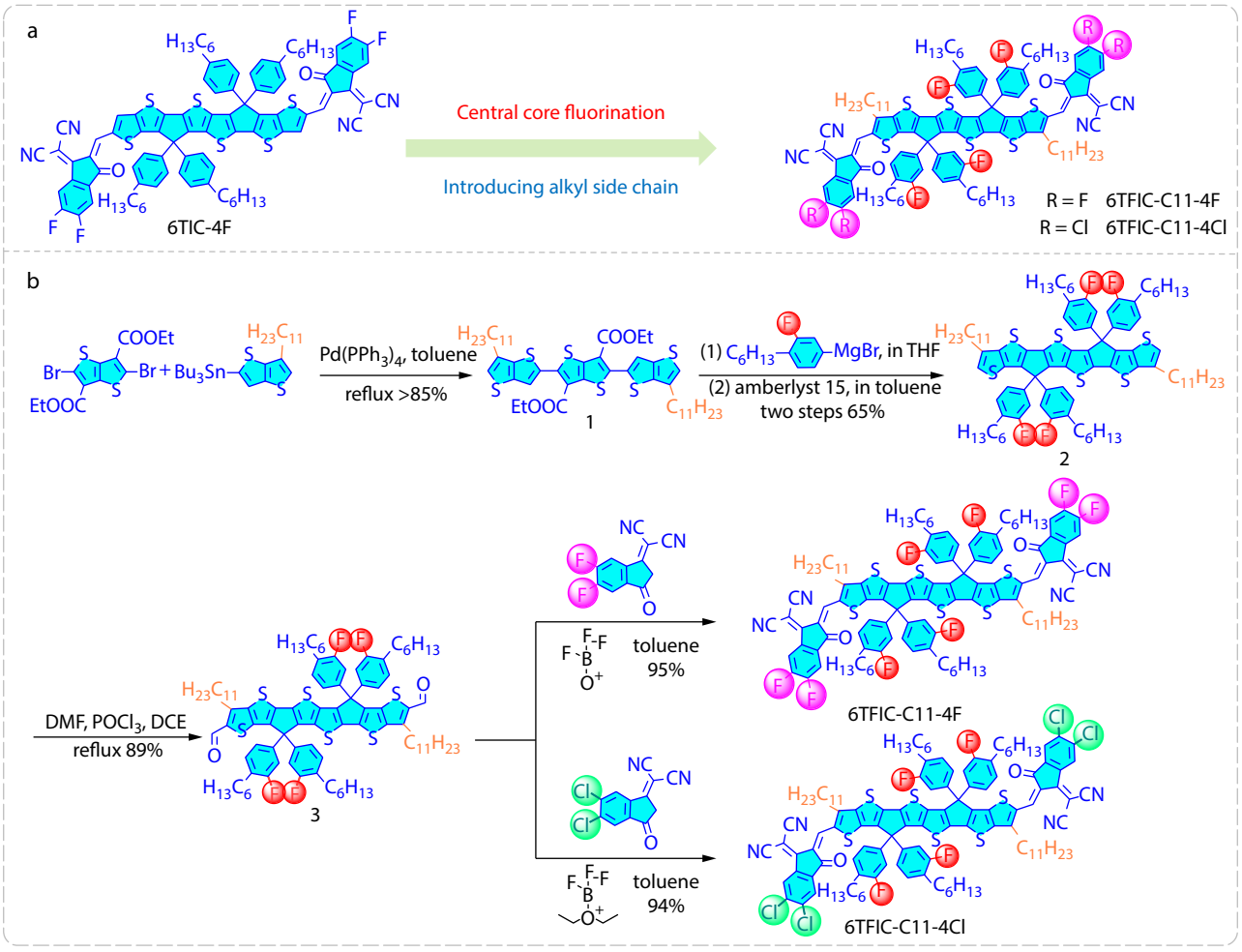

Fig. 2 (a) Chemical structures and (b) synthetic routes of the two novel acceptors 6TFIC-C11-4F and 6TFIC-C11-4Cl.

ing in a stronger IEF. In addition, the PM6:6TFIC-C11-4Cl-based devices demonstrated reduced energy loss and a higher J_{SC}, validating the potential of terminal chlorination in designing high-performance MFREAs.

MATERIALS AND METHODS

Materials

All reagents were purchased from commercial sources and used without further purification. PM6 and the interfacial layer material PFN-Br were purchased from Solarmer Materials Inc. The solid additive 1,3-dibromo-5-chlorobenzene (DBCl) was obtained from Energy Chemicals. Indium-tin oxide (ITO) glasses were sourced from South China Science & Technology Co., Ltd. Chloroform (CF) was purchased from Sigma-Aldrich Inc., and silver (Ag) was supplied by Zhong Nuo Advanced Material Technology Co., Ltd.

Fabrication of OSC Devices

Traditional devices were fabricated in the configuration ITO/PEDOT:PSS/active layer/PFN-Br/Ag. The ITO-coated glass was sequentially cleaned by ultrasonic agitation in acetone, detergent, deionized water, and isopropanol, followed by plasma treatment for 3 min. Then, PEDOT:PSS (Baytron PVP 4083) was spin-cast on ITO glass at 4000 r·min^{-1} for 30 s and annealed at 150 °C for 20 min in air. The devices were transferred to a glove box filled with N_2. Active layer solutions (PM6:6TIC-4F weight ratio is 1:1.2) were prepared in CF. The total active layer solution concentration is 17.6 mg·mL^{-1} with 12 mg·mL^{-1} DBCl. The active layer solution was stirred for 3 h at 50 °C, and then the active layers were spin-coated from the PM6:6TIC-4F solution on the substrates at a spin-coating speed of 3000 r·min^{-1} after the solution cooled to room temperature. The blended film was thermally annealed at 110 °C for 10 min. Finally, the PFN-Br dissolved in methanol at a concentration of 0.5 mg·mL^{-1} was spin-coated on top of the active layer. The device fabrication was completed by depositing 100 nm of Ag in a vacuum chamber at 10^{-7} Torr. Typical cells have devices area of 0.04 cm^2, which is defined by a metal mask with an aperture aligned with the device area. The PM6:6TFIC-C11-4F and PM6:6TFIC-C11-4Cl devices were prepared in a manner similar to that for the PM6:6TIC-4F device.

RESULTS AND DISCUSSION

Synthesis and Characterization

The synthetic routes to 6TFIC-C11-4F and 6TFIC-C11-4Cl are presented in Fig. 2(b). Diethyl 6,6′-diundecyl-[2,2':5',2''-terthieno-[3,2-*b*]thiophene]-3',6'-dicarboxylate (Compound 1) was pre-

pared as reported in the literature.[42] Subsequent reaction of Compound 1 with the prepared Grignard reagent in tetrahydrofuran solvent and ring closure in the presence of amberlyst 15 gave 6TF-C11 (Compound 2). 6TF-C11 was subsequently formylated using the Vilsmeier-Haack reactions to give dialdehyde 6TF-C11-CHO (Compound 3). Finally, 6TFIC-C11-4F and 6TFIC-C11-4Cl were successfully obtained through Knoevenagel-condensations in 93%–95% yields. The chemical structures of all intermediates were confirmed by ^{1}H-NMR with 6TFIC-C11-4F and 6TFIC-C11-4Cl Which were further characterized by ^{1}H-NMR, ^{13}C-NMR and MALDI-TOF mass spectrometry (Figs. S1–S8 in the electronic supplementary information, ESI). Based on thermogravimetric analysis (TGA), the decomposition temperatures (5% weight loss temperature) of 6TFIC-C11-4F (312 °C) and 6TFIC-C11-4Cl (328 °C) are greater that of 6TIC-4F (298 °C), implying they are more thermally stable and have better application prospects (Fig. S9 in ESI).

Molecular Simulations and Single-crystal X-ray Diffraction Analysis

To investigate the influence of central-core side-chain fluorination on the electronic properties of the acceptors, density functional theory (DFT) calculations were performed at the B3LYP/6-31G(d,p) level to evaluate the electrostatic potential (ESP) distributions and overall average ESP ($\overline{V}$) of the three acceptors and PM6, as depicted in Figs. 3(a)–3(c) and Fig. S10 in ESI. Quantitative ESP analysis was conducted using the Multiwfn 3.8 (dev) program,[42–44] with detailed values summarized in Table 1 and Tables S1 and S2 (in ESI). Figs. 3(a)–3(c) show the predominantly blue and green surface ESP distributions for all three molecules, indicative of the positive electrostatic potentials characteristic of the acceptors. The introduction of fluorine atoms in the side chain and chlorine atoms at the terminal enhances electron-withdrawing ability, which is consistent with the calculated $\overline{V}$: 6TIC-4F (145.12 meV) < 6TFIC-C11-4F (157.26 meV) < 6TFIC-C11-4Cl (163.21 meV). To further highlight the impact of central-core side-chain fluorination on the ESP, we calculated the $\overline{V}$ of 6TIC-C11-4F. Compared to 6TIC-4F, 6TIC-C11-4F only introduces an additional linear C11 alkyl side chain on the thiophene unit. Notably, 6TFIC-C11-4F exhibited a larger $\overline{V}$ than 6TIC-C11-4F, clearly indicating that fluorination markedly enhanced its electron-withdrawing capability (Fig. S11 and Table S1 in ESI). For acceptors, a larger $\overline{V}$ correlates with stronger electron-deficient character and greater donor-acceptor ESP differences, leading to en-

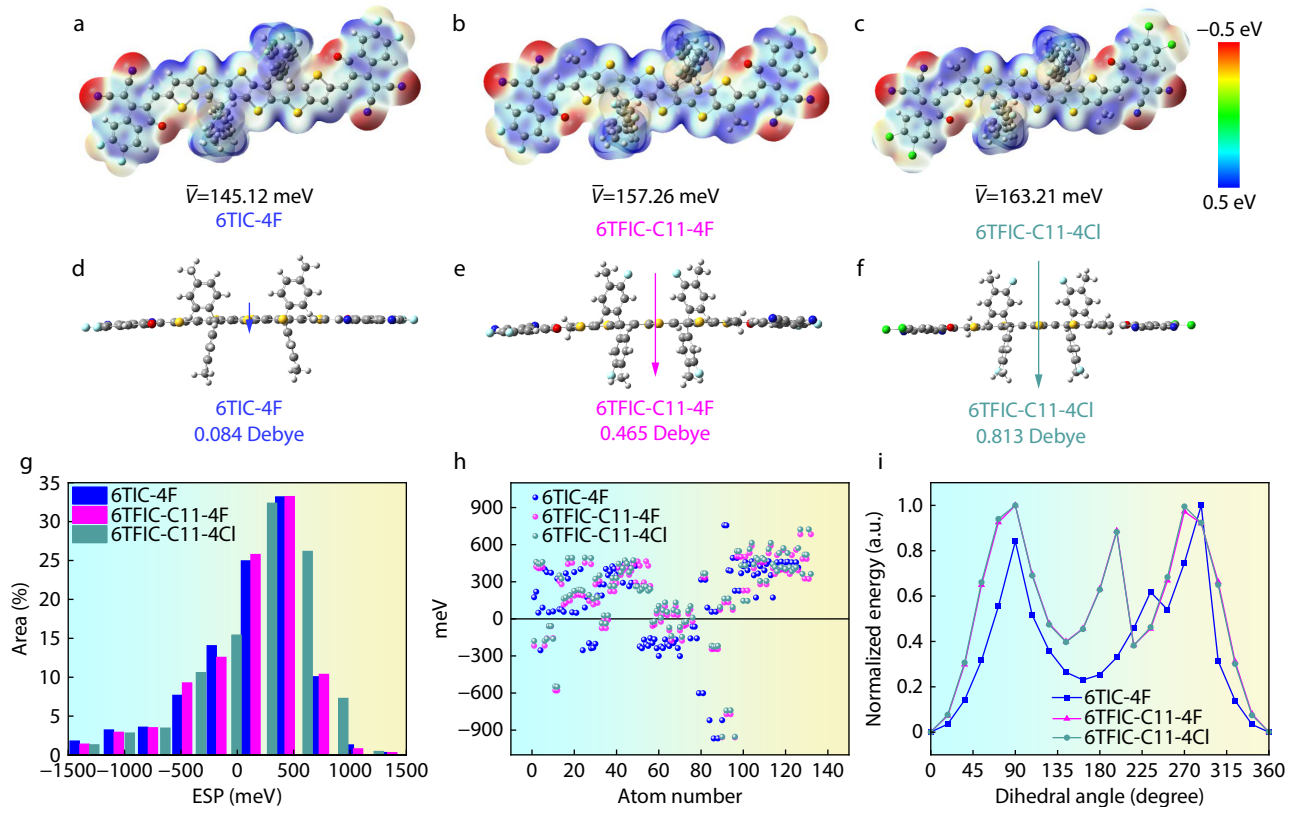

Fig. 3 ESP distributions and overall average values of ESP of (a) 6TIC-4F, 6 (b) TFIC-C11-4F, and (c) 6TFIC-C11-4Cl; (d–f) Side view and dipole moments of the three acceptors; (g) ESP area distributions, (h) average ESP value on each atom, and (i) total energy scans of the three acceptors.

Table 1 ESP parameters of 6TIC-4F, 6TFIC-C11-4F and 6TFIC-C11-4Cl.

Acceptor	Overall surface area (Å^2)	Minimal value (meV)	Maximal value (meV)	Overall average value (meV)
6TIC-4F	1126.05	−1513.26	1526.72	145.12
6TFIC-C11-4F	1160.95	−1506.49	1602.02	157.26
6TFIC-C11-4Cl	1213.85	−1507.33	1647.84	163.21

hanced IEF. Thus, 6TFIC-C11-4F and 6TFIC-C11-4Cl can form a stronger IEF with donors than 6TIC-4F, which is conducive to improving J_{SC}. Notably, this molecular design strategy is particularly advantageous for emerging optoelectronic devices, such as semi-transparent organic solar cells (ST-OSCs) and organic photodetectors (OPDs), where near-infrared II (NIR-II) acceptors with ultra-narrow bandgaps are commonly employed. In such systems, an insufficient energy-level offset often leads to poor exciton dissociation efficiency. Increasing the acceptor ESP *via* central-core side-chain fluorination is an effective approach to overcome this limitation. As shown in Figs. S12(a)–S12(c) (in ESI), the DFT calculation results indicate that alkyl side chain modification, central-core side-chain fluorination, and terminal chlorination have minimal effects on molecular coplanarity, with all three acceptors exhibiting good molecular planarity. However, core fluorination and terminal chlorination significantly increase the molecular dipole moment (Figs. 3d–3f), which helped reduce the exciton binding energy and consequently suppressed non-radiative recombination losses (ΔE_3). Meanwhile, the large dipole moments of 6TFIC-C11-4F and 6TFIC-C11-4Cl indicate a more uneven intramolecular charge distribution, which is beneficial for strengthening the intermolecular interactions. This is further supported by their broader ESP spatial distributions and more dispersed atomic ESP maps compared with those of 6TIC-4F, as depicted in Figs. 3(g) and 3(h). Similarly, we also calculated the dipole moment of 6TIC-C11-4F, as well as its ESP spatial distributions and atomic ESP maps (Figs. S13 and S14 in ESI). As expected, 6TFIC-C11-4F exhibits a much larger dipole moment than 6TIC-C11-4F, indicating that central-core side-chain fluorination not only enhances $\overline{V}$ but also significantly increases the molecular dipole moment. Potential energy surface scans were performed on half-molecules of the three acceptors to assess the structural stability effects of core fluorination and terminal chlorination (Fig. 3i). 6TIC-4F exhibits two low-energy states at approximately 0° and 162°, suggesting the coexistence of multiple conformers. In contrast, 6TFIC-C11-4F and 6TFIC-C11-4Cl adopted only the 0° conformation as the global minimum because of steric and electronic effects. This enhanced conformational rigidity suggests improved structural stability, which is favorable for efficient charge transport.

To understand the effect of the central-core side-chain fluorination on the molecular geometry and packing arrangement, single crystal X-ray diffraction analysis was conducted. We attempted to cultivate single crystals of 6TFIC-C11-4F and 6TFIC-C11-4Cl. Eventually, single crystals were successfully obtained only for 6TFIC-C11-4F in a chloroform/methanol system *via* natural evaporation. The crystal structures of 6TIC-4F[18] and 6TFIC-C11-4F are shown in Fig. 4, with the crystal parameters listed in Table S3 (in ESI). The 6TIC-4F crystal is isostructural which belongs to the monoclinic system with space group C2/c, while 6TFIC-C11-4F is crystallized in the triclinic system with space group P-1. As shown in Figs. 4(a)–4(c), the intramolecular distances ($d_{intra,\ S\cdots O}$ = 2.70, 2.72 Å) are significantly shorter than the sum of the Van De Waals radius ($r_{W,\ S\cdots O}$ = 3.25 Å), suggesting the presence of intramolecular S…O noncovalent interactions. In besides, the $d_{intra,\ S\cdots O}$ of 6TFIC-C11-4F is slightly larger than that of 6TIC-4F, which is mainly attributed to the spatial site resistance of

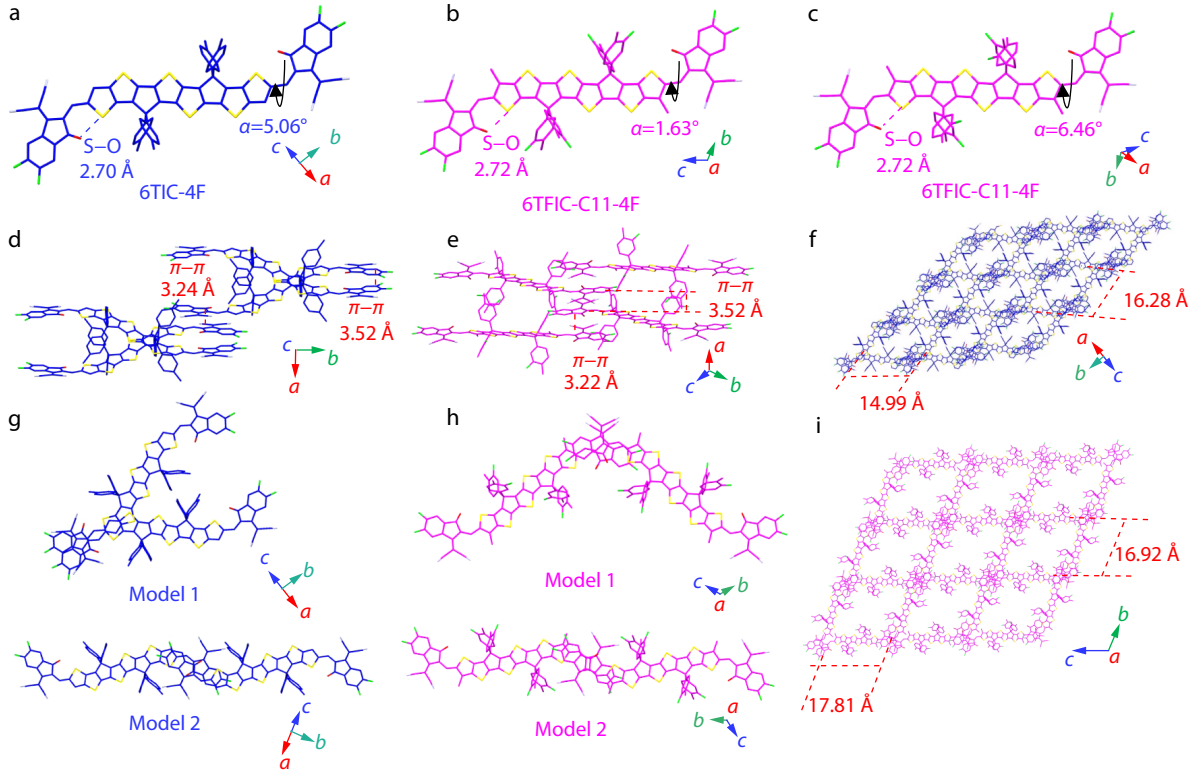

Fig. 4 The single crystallographic structures of (a) 6TIC-4F[18] (CCDC: 1818232), (b, c) 6TFIC-C11-4F (CCDC: 2355584); The detailed *π-π* stackings of (d) 6TIC-4F, and (e) 6TFIC-C11-4F; The molecular packing model of (f) 6TIC-4F and (g) 6TFIC-C11-4F; The 3D network packing of (h) 6TIC-4F, and (i) 6TFIC-C11-4F.

the alkyl chains. The dihedral angles (θ) between the central core and end-groups were 5.06° for 6TIC-4F, and 1.63° and 6.46° for the two conformations of 6TFIC-C11-4F. As shown in Fig. S15 (in ESI), 6TIC-4F and the second conformation of 6TFIC-C11-4F exhibited Z-curved geometries and planar molecular conformations, whereas the first conformation of 6TFIC-C11-4F displayed a planar geometric configuration. This suggests that fluorination and alkyl chain engineering enhance the molecular rigidity while diversifying the molecular conformation, which promotes more favorable π-π stacking. Further exploration of the self-assembly behavior of the two acceptors revealed that both 6TIC-4F and 6TFIC-C11-4F relied on two stacking models (Figs. 4d–4g). In the 6TIC-4F crystal, two distinct dimers are formed through intermolecular π-π interactions, exhibiting stacking distances ($d_{\pi\text{-}\pi}$) of 3.52 Å in Model 1 and 3.24 Å in Model 2. Compared to 6TIC-4F, the dimers within the 6TFIC-C11-4F crystal are formed *via* stronger π-π interactions ($d_{\pi\text{-}\pi}$ = 3.52 Å and 3.22 Å), and it also has a greater overlap of π-π stacking. Additionally, the stacking factor (SF) is widely used in single crystals to clearly compare the variation of different acceptor packing, which is defined as the product of the horizontal and vertical distances in a lattice. As shown in Figs. 4(h) and 4(i), 6TFIC-C11-4F exhibited a significantly larger SF value (301.25) than 6TIC-4F (244.04), likely due to the introduction of long alkyl side chains. Although a smaller SF value is generally associated with tighter molecular packing and potentially better charge transport, this correlation does not always hold in systems where multiple structural and morphological factors interact. In the present case, the long alkyl chains may fill the honeycomb-like cavities and reduce the free volume, thereby weakening the electron-phonon coupling and lowering the energetic disorder. The side chains may also enhance intermolecular interactions, collectively improving charge transport (*vide infra*).

Electrochemical and Optical Properties

Both the intramolecular charge transfer (ICT) effect and intermolecular interactions significantly influence molecular absorption. Given that core fluorination slightly weakens the ICT effect and modulates the molecular packing behavior (as discussed above), ultraviolet-visible-near-infrared (UV-Vis-NIR) spectroscopy was employed to investigate the resulting absorption characteristics, as shown in Fig. 5(a), and the detailed parameters are summarized in Table 2. In solution, the maximum absorption peaks of 6TIC-4F, 6TFIC-C11-4F and 6TIFC-C11-4F were located at 831, 814 and 858 nm, respectively. In the thin films, all three molecules showed red-shifted and broadened absorption spectra relative to their solution, suggesting stronger molecular packing in each film state. Specifically, compared with 6TIC-4F, 6TFIC-C11-4F showed a 17 nm blue shift in its maximum absorption peak, which can be attributed to the weakened ICT effect induced by core fluorination, consistent with the ESP calculation results. In contrast, terminal chlorination significantly enhanced the ICT effect, resulting in a 44 nm red shift for 6TFIC-C11-4Cl relative to 6TFIC-C11-4F, which is favorable for improving J_{SC}. Particularly, in ST-OSCs, increasing visible transmittance requires suppressing visible absorption, which reduces J_{SC}, while extending absorption into the near-infrared region often increases non-radiative recombination. This trade-off can be mitigated by central-core side-chain fluorination and terminal chlorination, which enhance the donor-acceptor IEF, thereby increasing J_{SC} without introducing additional E_{loss}. The optical bandgaps (E_g^{opt}) determined from the absorption onsets in thin films are 1.26, 1.35, and 1.30 eV for 6TIC-4F, 6TFIC-C11-4F, and 6TFIC-C11-4Cl, respectively. These results are consistent with cyclic voltammetry (CV) measurements (Fig. S16 in ESI and Fig. 5b) and DFT calculations (Fig. S17 in ESI). The LUMO and HOMO energy levels of 6TIC-4F, 6TFIC-C11-4F, and 6TFIC-C11-4Cl were determined to be −4.03/−5.51, −3.98/−5.58, and −4.05/−5.57 eV, respectively, with 6TIC-4F values agreeing well with literature reports (Table 2). Both 6TFIC-C11-4F and 6TFIC-C11-4Cl exhibited downshifted HOMO levels compared with 6TIC-4F, indicating that core fluorination effectively enhances the exciton dissociation driving force.

Photovoltaic Performance

To investigate the photovoltaic properties of 6TIC-4F, 6TFIC-C11-4F, and 6TFIC-C11-4Cl, OSCs with conventional ITO/PEDOT:PSS/active layer/PFN-Br/Ag structure were fabricated (Fig. 5c). PM6 was selected as the donor because of its complementary absorption and suitable energy-level alignment with acceptors. The active layers were processed from CF using a dynamic drop-casting method, which has been widely applied in Y6-based systems to accelerate crystallization and promote a thermodynamically optimized film morphology. All the devices were prepared under identical conditions with a donor-to-acceptor ratio of 1:1.2 and a solution concentration of 12 mg·mL^{-1} containing DBCl as an additive. The current density-voltage (*J-V*) characteristics of the optimized devices are shown in Fig. 5(d) and summarized in Table 3. The PM6:6TIC-4F-based device delivered a PCE of 10.52%, with a V_{OC} of 0.755 V, a J_{SC} of 20.71 mA·cm^{-2}, and a fill factor (FF) of 67.27%. In comparison, the device incorporating 6TFIC-C11-4F exhibited a higher V_{OC} of 0.784 V, a substantially enhanced J_{SC} of 24.24 mA·cm^{-2}, and an improved FF of 70.07%, leading to a significantly increased PCE of 13.32%. The pronounced enhancement in J_{SC} is primarily attributed to the higher $\bar{V}$ and enhanced molecular packing in the blend film of 6TFIC-C11-4F compared to 6TIC-4F, which generates a stronger IEF at the donor-acceptor interface and thereby facilitating exciton dissociation. Notably, the PCE of 13.3% is among the highest reported efficiencies for devices based on A-D-A narrow-bandgap acceptors. Further terminal chlorination led to a PM6:6TFIC-C11-4Cl-based device, which shows a slightly increased V_{OC} of 0.789 V and a further enhanced J_{SC} of 24.91 mA·cm^{-2}. This additional improvement in J_{SC} was associated with the higher $\bar{V}$ of 6TFIC-C11-4Cl, resulting in an even stronger IEF when blended with PM6. However, despite these advantages, the FF of the PM6:6TFIC-C11-4Cl-based device decreases significantly to 62.57%, ultimately limiting its PCE to 12.30%. The reduced FF may originate from excessive molecular aggregation and less favorable phase separation induced by terminal chlorination, which can deteriorate the charge-transport balance (*vide infra*). Interestingly, although 6TFIC-C11-4Cl possesses a deeper LUMO energy level (−4.05 eV) than 6TFIC-C11-4F (−3.98 eV), the corresponding device exhibits a higher V_{OC}, implying reduced energy loss, which is discussed in detail in the energy loss analysis section. Consistent with the enhanced J_{SC} discussed above, the EQE spectra shown in Fig. 5(e) reveal that devices based on 6TFIC-C11-4F and 6TFIC-C11-4Cl exhibit-

https://doi.org/10.1007/s10118-026-3655-0

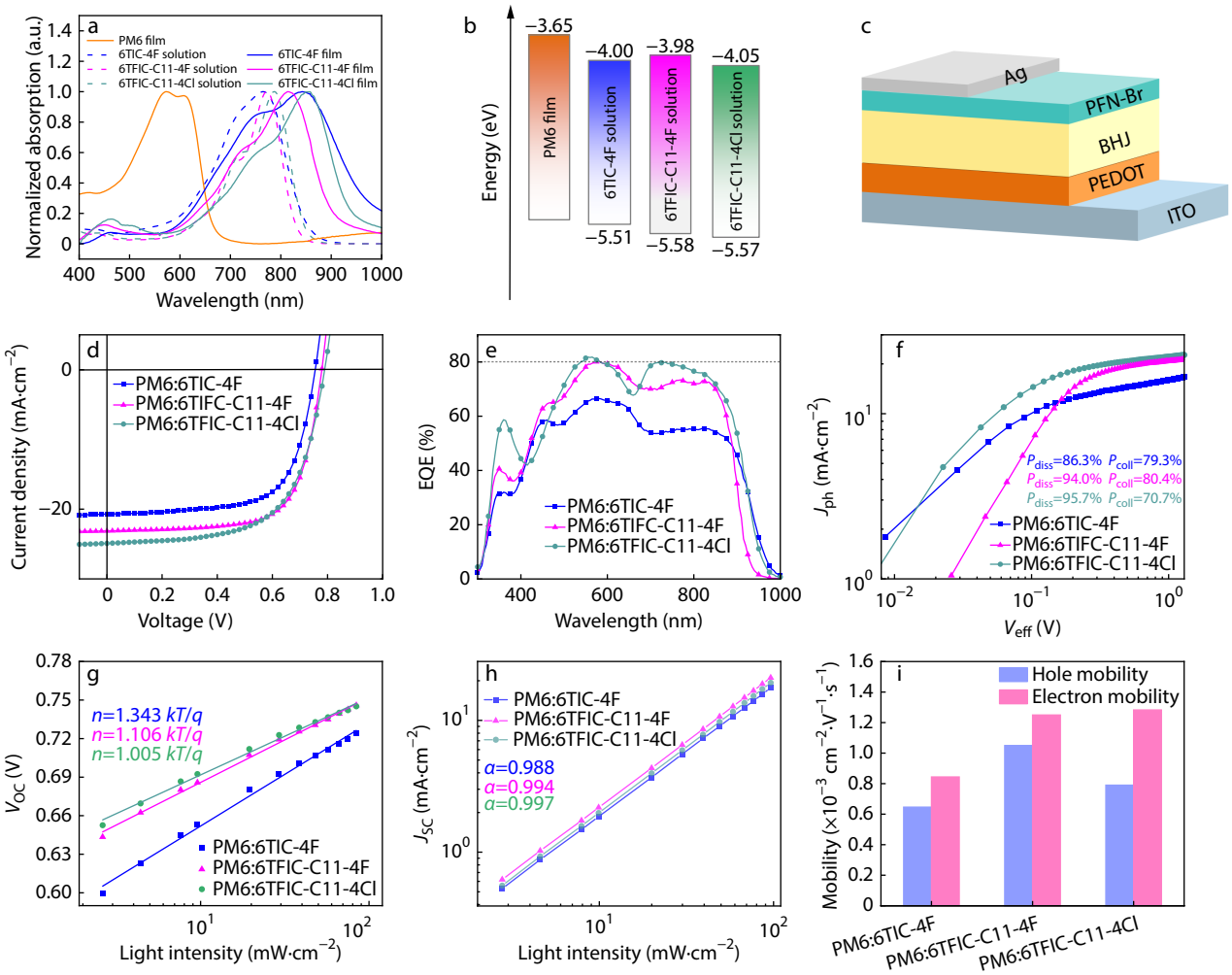

Fig. 5 (a) UV-Vis-NIR absorption spectra of PM6, 6TIC-4F, 6TFIC-C11-4F and 6TFIC-C11-4Cl; (b) The energy level diagrams of the materials; (c) The OSCs device architecture; (d) *J-V* characteristics of PM6:6TIC-4F, PM6:6TFIC-C11-4F and PM6:6TFIC-C11-4Cl-based devices; (e) EQE spectra; (f) J_{ph}-V_{eff} curves; (g) J_{SC}-P_{light}; (h) V_{OC}-P_{light} characteristics of devices based on PM6:6TIC-4F, PM6:6TFIC-C11-4F and PM6:6TFIC-C11-4Cl; (i) Measurement of hole and electron mobilities of the PM6:6TIC-4F, PM6:6TFIC-C11-4F and PM6:6TFIC-C11-4Cl blend films using SCLC method.

Table 2 The optical and electrochemical properties of the three small molecules.

Acceptor	λ_{max}[a] (nm)	λ_{onset}[a] (nm)	λ_{max}[b] (nm)	λ_{onset}[b] (nm)	E_g[c] (eV)	E_{HOMO}[d] (eV)	E_{LUMO}[d] (eV)	E_g[e] (eV)
6TIC-4F	765	873	831	988	1.26	−5.51	−4.03	1.48
6TFIC-C11-4F	772	835	814	920	1.35	−5.58	−3.98	1.60
6TFIC-C11-4Cl	786	852	858	956	1.30	−5.57	−4.05	1.52

[a] In chloroform solution; [b] in neat film; [c] calculated from the empirical formula $E_g = 1240/\lambda_{onset}$[b]; [d] measured by cyclic voltammetry (CV) method; [e] calculated from equation $E_g = E_{HOMO}$[d] − E_{LUMO}[d].

Table 3 Summary of photovoltaic parameters for different devices under the illumination of AM 1.5 G, 100 mW·cm^{-2}.

Active layer	V_{OC} (V)	J_{SC} (mA·cm^{-2})	FF (%)	PCE[a] (%)
PM6:6TIC-4F	0.755	20.71	67.27	10.52 (10.29±0.23)
PM6:6TFIC-C11-4F	0.784	24.24	70.07	13.32 (13.13±0.19)
PM6:6TFIC-C11-4Cl	0.789	24.91	62.57	12.30 (12.05±0.25)

[a] Average values with standard deviation in parentheses were obtained from 10 devices.

ed markedly higher photoresponses across the main absorption region compared with the 6TIC-4F-based device, further confirming the effectiveness of core fluorination and terminal chlorination in improving photocurrent generation. The integrated J_{SC} values derived from the EQE spectra are 19.84, 23.47, and 24.82 mA·cm^{-2} for the PM6:6TIC-4F, PM6:6TFIC-C11-4F, and PM6:6TFIC-C11-4Cl devices, respectively. These values are in good agreement with those obtained from the *J-V* measurements, with deviations of less than 5%, demonstrating the reliability of the photovoltaic characterization.

https://doi.org/10.1007/s10118-026-3655-0

To elucidate the origins of the differences in J_{SC} and FF among the three OSC devices, the exciton dissociation, charge transport, and recombination behaviors were systematically investigated. The exciton dissociation probability (P_{diss}) was evaluated from the relationship between the photocurrent density (J_{ph}) and the effective voltage (V_{eff}).[45,46] The J_{ph} is defined as $J_{ph} = J_L - J_D$, where J_L and J_D denote the current densities under illumination and in the dark, respectively. V_{eff} is given by $V_{eff} = V_0 - V_{bias}$, where V_0 corresponds to the voltage at which J_{ph} equals zero and V_{bias} is the applied bias voltage. P_{diss} is determined by normalizing J_{ph} to the saturation photocurrent density (J_{sat}) obtained under sufficiently high V_{eff}. As shown in Fig. 5(f), the extracted P_{diss} values were 86.3%, the PM6:6TIC-4F-based device, 94.0% for the PM6:6TFIC-C11-4F-based device and 95.7% for the PM6:6TFIC-C11-4Cl-based device. The substantially higher P_{diss} values observed for the devices incorporating core-fluorinated acceptors indicate more efficient exciton dissociation, which directly contributes to the enhanced J_{SC} discussed above. This trend is consistent with the DFT calculation results, further confirming that central-core side-chain fluorination effectively promotes charge separation at the donor-acceptor interface. The charge recombination behaviors of the devices were further examined by analyzing the dependence of V_{OC} and J_{SC} on the light intensity (P_{light}). The relationship between V_{OC} and P_{light} can be described by $V_{OC} \propto (nkT/q)\ln(P_{light})$, where k is Boltzmann's constant, T is the absolute temperature, and q is the elementary charge. As depicted in Fig. 5(g), the slope factors extracted for the PM6:6TIC-4F, PM6:6TFIC-C11-4F, and PM6:6TFIC-C11-4Cl-based devices were 1.343, 1.106, and 1.005 kT/q, respectively, revealing that trap-assisted recombination can be substantially suppressed in devices incorporating core-fluorinated acceptors. In contrast, the P_{light} dependence of J_{SC} can be expressed as $J_{SC} \propto (P_{light})^{\alpha}$, where the exponent α characterizes the degree of bimolecular recombination. As shown in Fig. 5(h), the α values for the PM6:6TIC-4F, PM6:6TFIC-C11-4F, and PM6:6TFIC-C11-4Cl-based devices were 0.988, 0.997, and 0.997, respectively. The α values approaching unity suggest that bimolecular recombination is negligible and comparable among the three devices, implying that the differences in device performance mainly originate from trap-assisted recombination rather than bimolecular recombination. Furthermore, the charge transport properties were evaluated *via* the space-charge-limited current (SCLC) technique by the fabrication of hole-only and electron-only devices (Fig. 5(i), Fig. S18, and Table S4 in ESI).[47] The calculated hole (μ_h) and electron (μ_e) mobilities for PM6:6TIC-4F, PM6:6TFIC-C11-4F and PM6:6TFIC-C11-4Cl were 0.646, 0.844, 1.05, 1.25, and 0.79/1.283 × 10^{-3} $cm^2 \cdot V^{-1} \cdot s^{-1}$, respectively, corresponding to μ_e/μ_h ratios of 1.307, 1.19 and 1.624. Among them, the PM6:6TFIC-C11-4F-based device exhibited the most well-balanced charge transport, which is consistent with the highest FF observed in the photovoltaic measurements. In contrast, the PM6:6TFIC-C11-4Cl-based device exhibited the most unbalanced charge transport among the three systems, which likely led to enhanced space-charge accumulation and carrier recombination under the operating conditions, thereby explaining its lowest FF despite the suppressed trap-assisted recombination.

Morphology and Crystallinity Characterization

The morphology of the blend films plays a crucial role in governing the charge generation, transport, and recombination processes in OSCs and thus directly determines the device performance. In view of the distinct variations in J_{SC} and FF discussed above, a systematic morphological investigation focusing on structural order and phase separation was conducted using transmission electron microscopy (TEM) and two-dimensional grazing-incidence wide-angle X-ray scattering (2D-GIWAXS). As shown in the TEM images (Figs. 6a–6c), the PM6:6TFIC-C11-4F and PM6:6TFIC-C11-4Cl blend films exhibit more pronounced fibrous features and well-developed interpenetrating network structures than the PM6:6TIC-4F blend film, suggesting more favorable phase separation for charge transport. Further insight into molecular packing was obtained from 2D-GIWAXS measurements, and the corresponding patterns and one-dimensional (1D) line-cut profiles shown in Figs. 6(d)–6(g). All blend films displayed pronounced diffraction features in the out-of-plane (OOP) direction, indicating a dominant face-on molecular orientation that is beneficial for vertical charge transport. The (010) OOP diffraction peaks of PM6:6TIC-4F, PM6:6TFIC-C11-4F, and PM6:6TFIC-C11-4Cl blend films are located at 1.76, 1.76, and 1.77 $Å^{-1}$, respectively, corresponding to similar π-π stacking distances of 3.57, 3.57, and 3.55 Å. Quantitative analysis of the 1D line-cut profiles (Fig. 6g and Table S5 in ESI) revealed that the crystal coherence lengths (CCLs) of the PM6:6TIC-4F, PM6:6TFIC-C11-4F, and PM6:6TFIC-C11-4Cl blend films were 36.0, 37.7, and 37.0 Å, respectively. The increased CCL observed for the PM6:6TFIC-C11-4F blend film indicates improved crystalline order and enhanced intermolecular packing, which is in good agreement with its more balanced charge transport and highest FF among the three devices. These results demonstrate that central-core side-chain fluorination effectively optimizes molecular packing, thereby facilitating charge transport and boosting the photovoltaic performance. In contrast, although the PM6:6TFIC-C11-4Cl blend film maintained a relatively large CCL, a slight reduction compared to the fluorinated analog was observed. This may originate from the substitution of fluorine with chlorine atoms, which introduces larger steric hindrance and increased intermolecular site resistance, leading to weakened noncovalent interactions. Such structural perturbations can adversely affect the charge transport balance, rationalizing the reduced FF observed in the PM6:6TFIC-C11-4Cl-based device despite its enhanced J_{SC}.

The morphology and molecular crystallinity are closely related to the film formation process. Therefore, *in situ* UV-Vis absorption spectroscopy was performed, as shown in Fig. 7. This technique provides time-resolved information on the evolution of absorption profiles during film formation, enabling a deeper understanding of how central-core side-chain fluorination and end-group chlorination influence the intramolecular interactions and crystallization kinetics in the active layers. The peak-position evolution of the active-layer films can be resolved into three distinct stages based on in-situ UV-Vis spectroscopy. In the initial stage, solvent evaporation dominated, leading to a gradual increase in solute concentration. In the second stage, the system reached saturation, triggering rapid molecular aggregation and nucleation, which was accompanied by a pronounced redshift of the ac-

https://doi.org/10.1007/s10118-026-3655-0

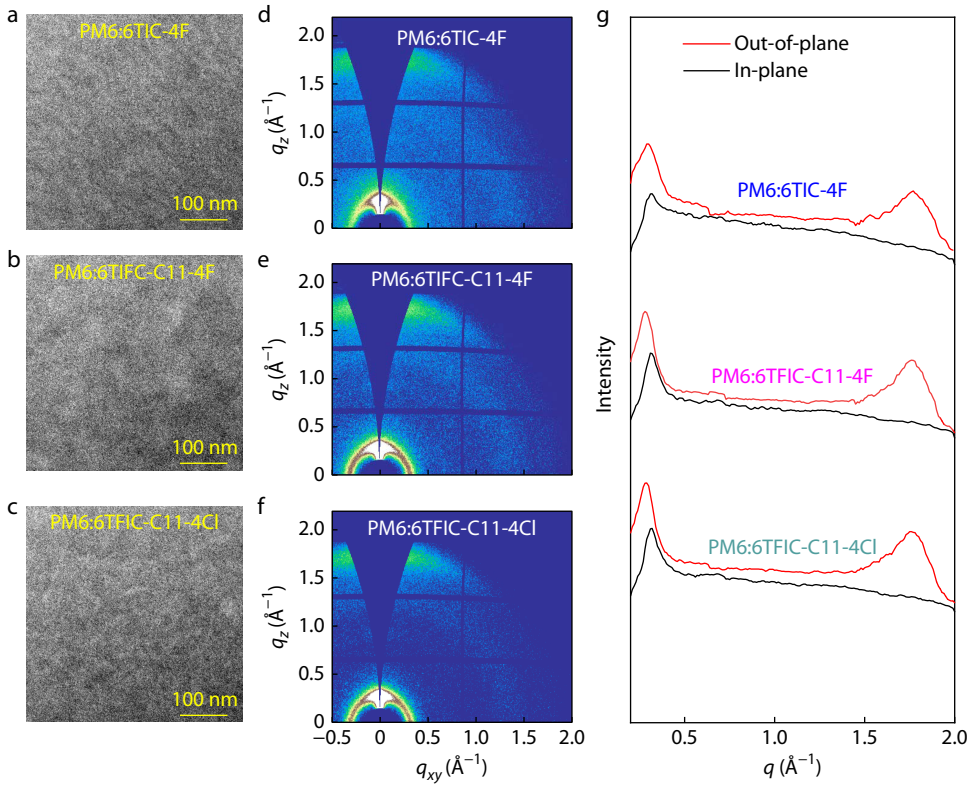

Fig. 6 (a–c) TEM images of the three blend films; (d–f) 2D-GIWAXS patterns for images of the three blend films; (g) corresponding in-plane (black) and out-of-plane (red) cut line profiles.

ceptor absorption peak. In the final stage, the acceptor peak position stabilizes, indicating that the film morphology essentially reached equilibrium.[48] As shown in Figs. 7(a)–7(i), the characteristic absorption peaks of the three acceptors were tracked as indicators of film evolution. When chlorobenzene was used as the processing solvent, the PM6:6TFIC-C11-4F blend film exhibited a longer crystallization nucleation time (1.0 s) than that of the PM6:6TIC-4F blend film (0.8 s). The prolonged nucleation process suggests the formation of a higher crystallinity and more ordered molecular stacking, which is favorable for charge transport. This observation is in good agreement with the increased CCL and improved molecular ordering revealed by GIWAXS measurements. In contrast, the PM6:6TFIC-C11-4Cl blend film exhibited a shorter nucleation time (0.9 s) than that of PM6:6TFIC-C11-4F. This relatively faster crystallization process indicates weaker crystallization kinetics and less ordered molecular stacking, which is consistent with its slightly reduced CCL. It should be noted that the initial rapid solvent evaporation stage was difficult to resolve because of the narrow time window. Therefore, chlorobenzene was employed to slow down the drying process and enable reliable *in situ* UV-Vis measurements. As shown in Fig. S19 (in ESI), similar *in situ* UV-Vis experiments conducted using chloroform as the solvent exhibited similar trends, further confirming the reliability of the observed crystallization behavior.

Charge Carrier Dynamics Analysis

Furthermore, the observed differences in the morphology and crystallinity among these blend films imply that their charge separation and transport dynamics merit further investigation. To this end, the carrier dynamics of the blends were analyzed using a time-resolved confocal imaging system (TRCIS), which integrates photoluminescence intensity mapping, lifetime imaging, and carrier lifetime distribution analysis to comprehensively evaluate the charge transfer processes. Compared to conventional photoluminescence (PL) and time-resolved PL (TR-PL) spectroscopy, TRCIS enables large-area acquisition of PL intensity and lifetime distributions with high spatial resolution, thereby minimizing errors arising from film inhomogeneity. The corresponding lifetime images and statistical histograms of the acceptor neat films are shown in Fig. S20 (in ESI) and Fig. 8. Under 780 nm excitation, the neat films of 6TIC-4F, 6TFIC-C11-4F, and 6TFIC-C11-4Cl, as well as all corresponding blend films, exhibited smooth surfaces and uniform fluorescence intensity (Figs. S20a–S20c in ESI and Figs. 8a–8c). The neat films of 6TIC-4F, 6TFIC-C11-4F, and 6TFIC-C11-4Cl exhibit relatively long average PL lifetimes of 0.995, 0.924 and 1.029 ns, respectively (Figs. S20d–S20i in ESI). In contrast, all blend films showed significantly reduced PL lifetimes, indicating efficient hole transfer at the donor-acceptor interfaces. Notably, the variations in the exciton lifetimes of the blend films are consistent with the trends observed in their PL intensity distributions. Specifically, a smaller difference in the overall average PL value corresponds to a shorter exciton lifetime, reflecting a more efficient exciton dissociation. Consequently, the side-chain fluorinated systems exhibited shorter exciton lifetimes, further confirming their better charge separation efficiency. Overall, the TRCIS results verify that the charge-transfer process is closely correlated with the intermolecular electrostatic environment and spatial homogene-

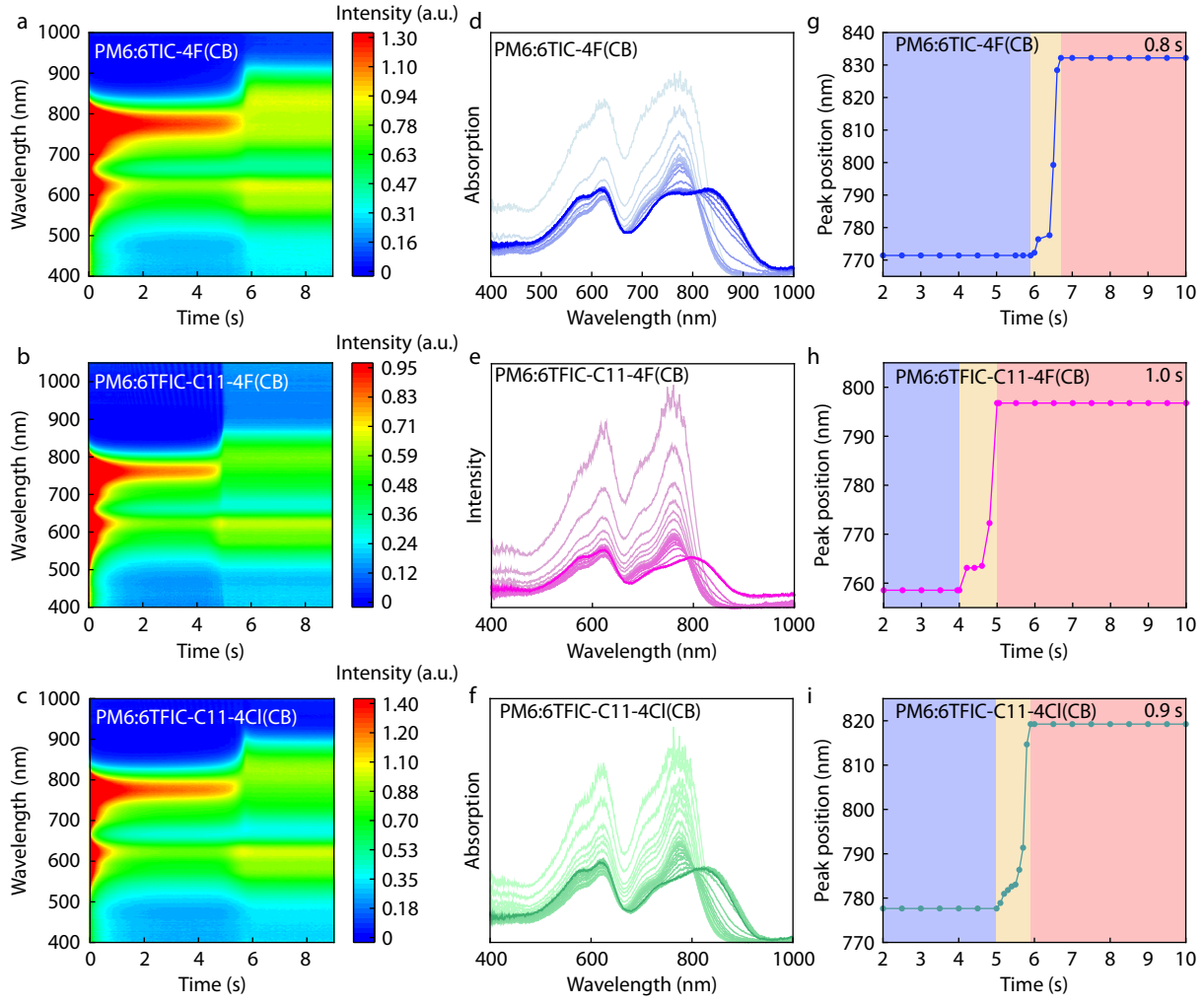

Fig. 7 The time-resolved spectra in the films of (a) PM6:6TIC-4F, (b) PM6:6TFIC-C11-4F and (c) PM6:6TFIC-C11-4Cl; The *in situ* UV-Vis absorption line profiles in the films of (d) PM6:6TIC-4F, PM6:6TFIC-C11-4F (e) and (f) PM6:6TFIC-C11-4Cl; The peak position evolution as a function of time of the acceptors in the films of (g) PM6:6TIC-4F, (h) PM6:6TFIC-C11-4F, and (i) PM6:6TFIC-C11-4Cl.

ity of the active layer. Through central-core fluorination and terminal chlorination, a stronger intermolecular electric field was established, which effectively promotes exciton dissociation and charge transport, leading to an enhanced J_{SC}. This provides a direct kinetic explanation for the superior photovoltaic performance of the PM6:6TFIC-C11-4F- and PM6:6TFIC-C11-4Cl-based devices compared with that of the PM6:6TIC-4F-based device.

Energy Loss Analysis

To further elucidate the origin of the energy loss (E_{loss}) in relation to the intermolecular interactions discussed above, Fourier-transform photocurrent spectroscopy external quantum efficiency (FTPS-EQE) and electroluminescence external quantum efficiency (EQE_{EL}) measurements were employed to quantitatively analyze E_{loss} (Fig. 9). As reported in the literature [49] the total E_{loss} in OSCs can be decomposed into three contributions. The first term, $\Delta E_1 = E_{gap} - qV_{OC}^{SQ}$, originates from the radiative recombination associated with above-bandgap absorption. The second term, $\Delta E_2 = qV_{OC}^{SQ} - qV_{OC}^{rad}$, corresponds to the radiative recombination induced by the sub-bandgap absorption. The third component, $\Delta E_3 = qV_{OC}^{rad} - qV_{OC} = -kT\ln(EQE_{EL})$, represents non-radiative recombination losses. The band gaps (E_g) of the blend films were determined from the intersection of their electroluminescence (EL) and normalized absorption spectra, as shown in Table 4, Fig. 9 and Fig. S21 (in ESI). Owing to the similar E_{gap} values, the ΔE_1 terms of the three systems are nearly identical, all around 0.26 eV. Likewise, the ΔE_2 values were relatively small and fell within a narrow range of 0.034–0.047 eV, consistent with their comparable Urbach energies (Figs. 9e–9g), indicating minimal variation in sub-bandgap radiative losses among the devices. As shown in Fig. 9(h), upon central-core fluorination, the EQE_{EL} of the PM6:6TFIC-C11-4F-based device decreased compared with that of PM6:6TIC-4F, leading to a slight increased ΔE_3. This suggests that although core fluorination strengthens the donor–acceptor intermolecular electric interactions and promotes charge separation, it simultaneously introduces additional non-radiative recombination pathways. Such behavior is likely associated with the increased contribution of charge-transfer (CT) excited states induced by fluorination of the central core, which generally exhibits higher non-radiative decay rates.[50,51] Notably, previous studies have demonstrated that terminal chlorination is an effective strategy for suppressing ΔE_3 and reducing ΔE_3 in OSCs.[37] Consistent with these reports, the PM6:6TFIC-C11-4Cl-based device exhibited a signifi-

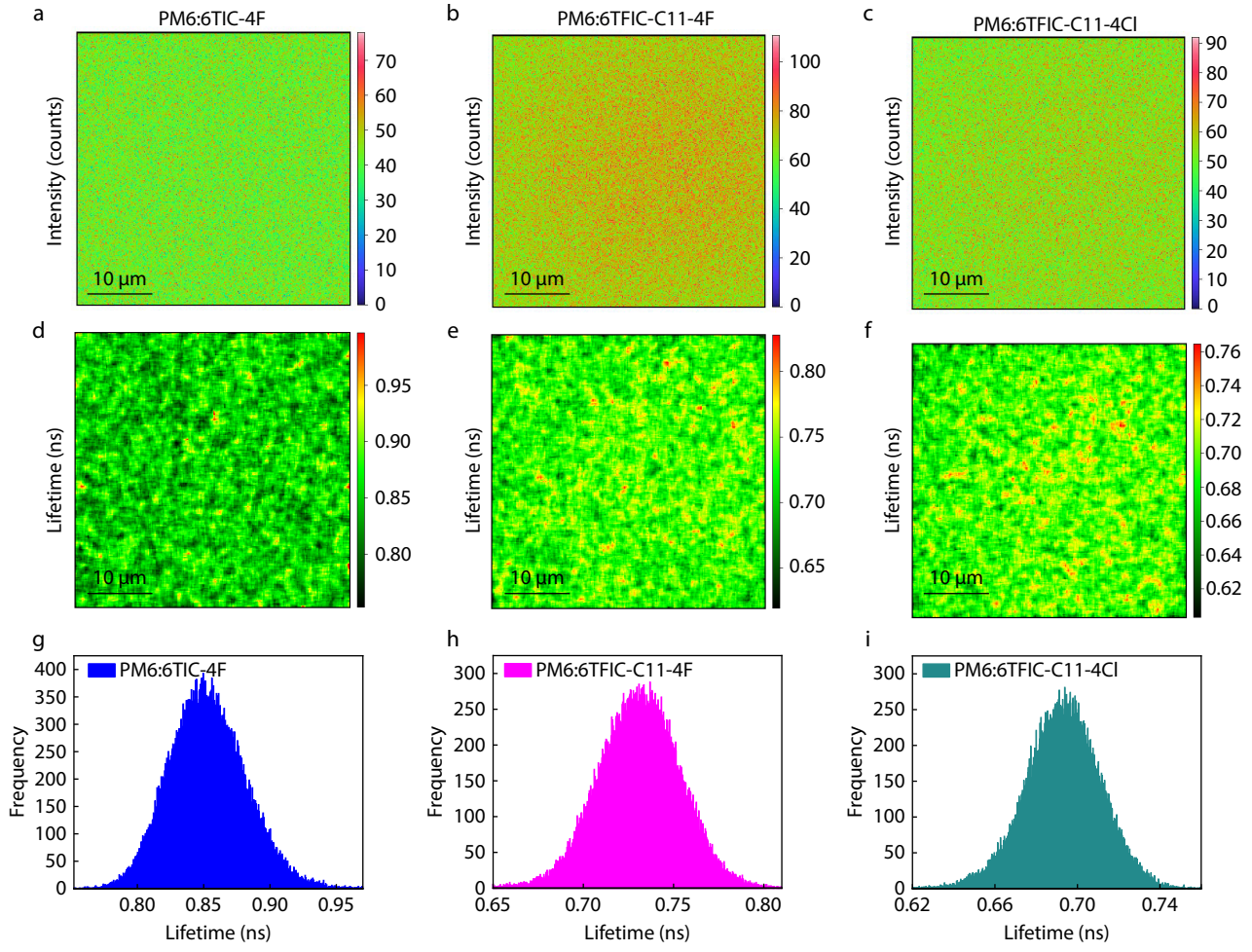

Fig. 8 The time-resolved confocal imaging (excitation at 780 nm). The photoluminescence of (a) PM6:6TIC-4F, (b) PM6:6TFIC-C11-4F, and (c) PM6:6TFIC-C11-4Cl blend films; (d–f) Lifetime imaging of the three blend films, and (g–i) the corresponding histogram of lifetime distribution.

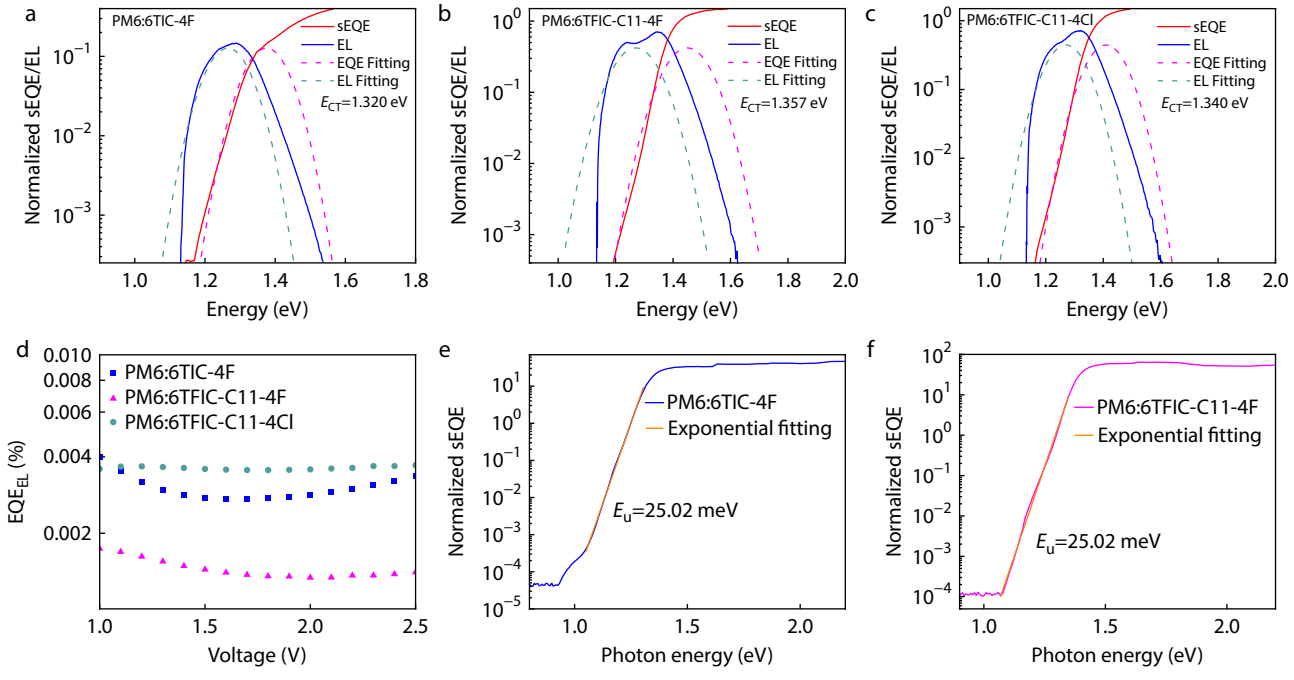

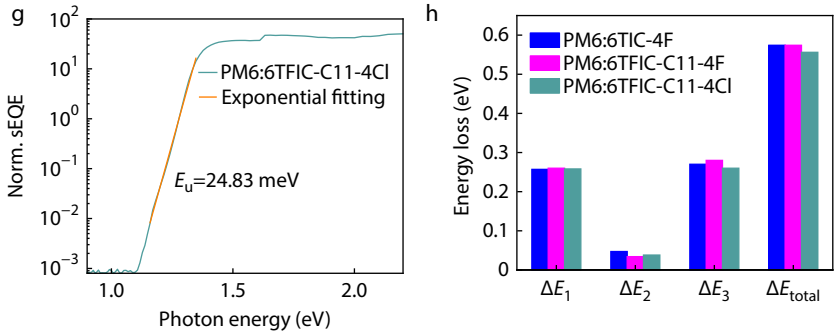

Fig. 9 (a–c) The normalized s-EQE and EL data for different blended devices; (d) EQE_{EL} of three devices; (e–g) Urbach energy of different blend devices; (h) The histogram of energy loss for different devices.

Table 4 Detailed energy loss of the OSCs based on different devices.

Donor	Acceptor	E_g (eV)	qV_{OC} (eV)	$qV_{OC,cal}$ (eV)	E_{loss} (eV)	ΔE_1 (eV)	ΔE_2 (eV)	ΔE_3 (eV)
PM6	6TIC-4F	1.327	0.763	0.753	0.574	0.257	0.047	0.270
	6TFIC-C11-4F	1.380	0.784	0.806	0.574	0.260	0.034	0.280
	6TFIC-C11-4Cl	1.352	0.789	0.796	0.556	0.258	0.038	0.260

cantly higher EQE_{EL} than that of the PM6:6TFIC-C11-4F-based device, resulting in a substantially reduced ΔE_3 of 0.260 eV. Overall, E_{loss} analysis revealed that while core fluorination enhanced donor-acceptor electric interactions and improved charge separation, it concomitantly increased E_{loss}, primarily through an enlarged ΔE_3. In contrast, terminal chlorination effectively counterbalances this drawback by suppressing non-radiative recombination. Therefore, the rational regulation of ΔE_3 through synergistic core and terminal-group engineering is essential for further improving the efficiency of fused-thiophene-based acceptors in OSCs.

CONCLUSIONS

In summary, this work addresses the intrinsic limitations of multithiophene fused-ring electron acceptors (MFREAs) in organic solar cells (OSCs), namely insufficient exciton dissociation efficiency and pronounced energy loss. Starting with the benchmark acceptor 6TIC-4F, two fused-thiophene acceptors, 6TFIC-C11-4F and 6TFIC-C11-4Cl, were rationally designed and synthesized by synergistically integrating alkyl side-chain engineering, central-core side-chain fluorination, and terminal chlorination strategies. Density functional theory (DFT) calculations revealed that 6TFIC-C11-4F exhibited a significantly higher overall average molecular electrostatic potential ($\overline{V}$ = 157.26 meV) than 6TIC-4F (145.12 meV), thereby increasing the electrostatic potential difference with the PM6 donor and strengthening the donor-acceptor intermolecular electric field. Benefiting from central-core side-chain fluorination, single-crystal analysis confirmed enhanced π-π stacking in 6TFIC-C11-4F, which effectively facilitates charge transport. Notably, the exciton dissociation efficiency increases from 86.3% to over 94%, directly indicating a strengthened donor-acceptor intermolecular electric field. As a result, the PM6:6TFIC-C11-4F-based device delivered a markedly improved PCE of 13.32% compared with the PM6:6TIC-4F reference device (PCE = 10.52%). GIWAXS analysis further revealed enhanced crystallite coherence lengths in both the in-plane and out-of-plane directions, confirming that core fluorination simultaneously optimizes the molecular packing and charge-transport pathways, thereby accounting for the substantial enhancement in J_{SC}. Furthermore, terminal chlorination in 6TFIC-C11-4Cl further amplified the donor-acceptor electrostatic potential difference, leading to a higher J_{SC} of 24.91 mA·cm^{-2}. More importantly, terminal chlorination significantly suppresses non-radiative energy loss, reducing ΔE_3 to 0.26 eV, which is 0.02 eV lower than that of the PM6:6TFIC-C11-4F-based device. Overall, this work established dual-halogenation as a viable and general molecular design strategy for optimizing multithiophene-fused-ring electron acceptors, providing clear theoretical guidance for the development of next-generation high-efficiency OSCs materials.

Conflict of Interests

The authors declare no interest conflict.

Electronic Supplementary Information

Electronic supplementary information (ESI) is available free of charge in the online version of this article at http://doi.org/10.1007/s10118-026-3655-0.

Data Availability Statement

Data supporting the findings of this study are available from the corresponding author upon reasonable request.

ACKNOWLEDGMENTS

This work was financially supported by the National Natural Science Foundation of China (Nos. 52553004, 52333006, 22479066 and 52527804).

REFERENCES

1 Liu, M.; Zhu, P.; Lai, S.; Zhang, X.; Fu, Y.; Xue, L.; Liu, D.; Feng, K.; Lu, X.; Guo, X.; Liao, X.; Chen, Y. Regulating molecular structure of S,

Graphical Abstract

Modulating Molecular Electrostatic Potential Unlocks Efficient Exciton Dissociation in A-D-A-type Narrow Bandgap Acceptors-based Organic Solar Cells

Jin Li, Ping Jiang, Hao-Jia Ding, Ming-Tao Liu, Yue Zhen, Dan Liu, Jia-Nan Fang, Pei-Pei Zhu,Shen-Bo Zhu, Hua-Wei Hu, Xun-Fan Liao, and Yi-Wang Chen

Jiangxi Normal University; Donghua University; Gannan Normal University

This work demonstrates that central-core side-chain fluorination effectively enhances the molecular electrostatic potential of A-D-A-type narrow-bandgap fused-ring electron acceptors, leading to strengthened intermolecular interactions and efficient exciton dissociation, ultimately achieving a power conversion efficiency of 13.32%, which is among the highest performances in this category-based organic solar cells.

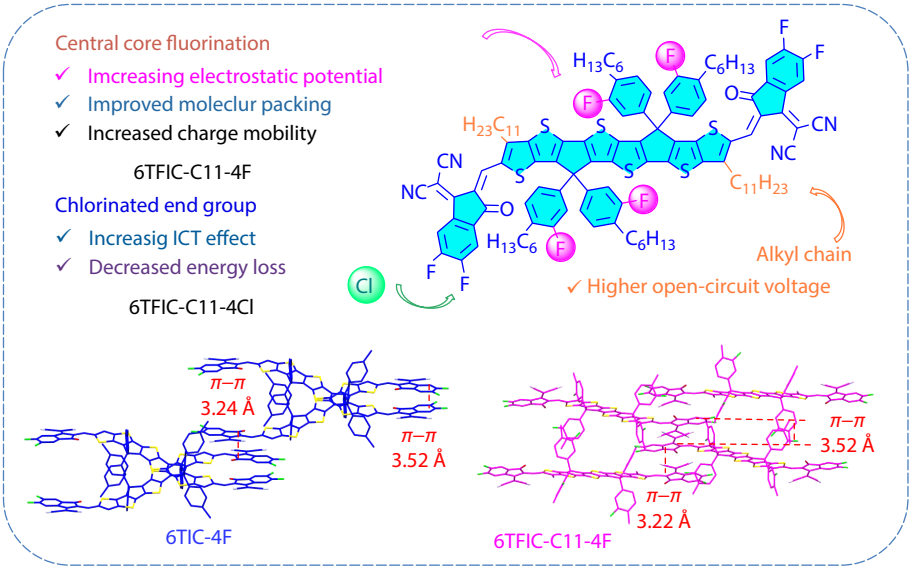

Chinese J. Polym. Sci. 2026, 44, 2534–2548 *https://doi.org/10.1007/s10118-026-3655-0*

N-heteroacene non-fullerene acceptors to achieve efficient photoelectric properties. *Chin. J. Chem*. **2025**, *43*, 13–22.

2 Zheng, X.; Wang, Y.; Chen, T.; Kong, Y.; Wu, X.; Zhou, C.; Luo, Q.; Ma, C. Q.; Zuo, L.; Shi, M.; Chen, H. Realizing record efficiencies for ultra-thin organic photovoltaics through step-by-step optimizations of silver nanowire transparent electrodes. *FlexMat* **2024**, *1*, 221–233.

3 Liao, X.; Liu, M.; Pei, H.; Zhu, P.; Xia, X.; Chen, Z.; Zhang, Y.; Wu, Z.; Cui, Y.; Xu, G.; Gao, M.; Ye, L.; Ma, R.; Liu, T.; Lu, X.; Zhu, H.; Chen, Y. Regulating crystallinity mismatch between donor and acceptor to improve exciton/charge transport in efficient organic solar cells. *Angew. Chem. Int. Ed.* **2024**, *63*, e202318595.

4 Ma, R.; Luo, Z.; Zhang, Y.; Zhan, L.; Jia, T.; Cheng, P.; Yan, C.; Fan, Q.; Liu, S.; Ye, L.; Zhang, G.; Xu, X.; Gao, W.; Wu, Y.; Wu, J.; Li, Y.; Liu, Y.; Liu, F.; Song, J.; Chen, H.; Chen, W.; Zhang, X.; Liu, Y.; Yuan, J.; Liu, Q.; Kan, Z.; Yin, H.; Li, X.; Ma, Y.; Deng, D.; Zhu, L.; Huo, Y.; Fan, B.; Fu, H.; Liao, X.; Hu, H.; Li, C.; Yu, R.; Hu, H.; Yao, Z.; Cai, Y.; Qian, D.; Cui, Y.; Yao, H.; Xu, B.; Kan, B.; Gao, K.; Duan, C.; Hu, X.; Sun, H. Organic solar cells: beyond 20%. *Sci. China Mater.* **2025**, *68*, 1689–1701.

5 Luo, X.; Yu, J.; Tang, H.; Cai, H.; Xiong, W.; Zhang, K.; Huang, F.; Cao, Y. Self-doped conjugated polymers with electron-deficient quinone units for enhanced electron transport in highly efficient organic solar cells. *FlexMat* **2024**, *1*, 105–115.

6 Li, X.; Kong, X.; Sun, G.; Li, Y. Organic small molecule acceptor materials for organic solar cells. *eScience* **2023**, *3*, 100171.

7 Nelson, J. Polymer: fullerene bulk heterojunction solar cells. *Mater. Today* **2011**, *14*, 462–470.

8 Zhao, J.; Li, Y.; Yang, G.; Jiang, K.; Lin, H.; Adel, H.; Ma, W.; Yan, H. Efficient organic solar cells processed from hydrocarbon solvents. *Nat. Energy* **2016**, *1*, 15027.

9 Huang, Y.; Kramer, E. J.; Heeger, A. J.; Bazan, G. C. Bulk heterojunction solar cells: morphology and performance relationships. *Chem. Rev.* **2014**, *114*, 7006–7043.

10 Zhao, W.; Ye, L.; Zhang, S.; Sun, M.; Hou, J. A universal halogen-free solvent system for highly efficient polymer solar cells. *J. Mater. Chem. A* **2015**, *3*, 12723–12729.

11 Lin, Y.; Wang, J.; Zhang, Z.; Bai, H.; Li, Y.; Zhu, D.; Zhan, X. An electron acceptor challenging fullerenes for efficient polymer solar cells. *Adv. Mater.* **2015**, *27*, 1170–1174.

12 Zhao, W.; Li, S.; Yao, H.; Zhang, S.; Zhang, Y.; Yang, B.; Hou, J. Molecular optimization enables over 13% efficiency in organic

solar cells. *J. Am. Chem. Soc.* **2017**, *139*, 7148−7151.
13 Xia, T.; Li, C.; Ryu, H. S.; Guo, J.; Min, J.; Woo, H. Y.; Sun, Y. Efficient fused-ring extension of A-D-A-type non-fullerene acceptors by a symmetric replicating core unit strategy. *Chem. Eur. J.* **2020**, *26*, 12411−12417.
14 Zhang, H.; Yao, H.; Hou, J.; Zhu, J.; Zhang, J.; Li, W.; Yu, R.; Gao, B.; Zhang, S.; Hou, J. Over 14% efficiency in organic solar cells enabled by chlorinated nonfullerene small-molecule acceptors. *Adv. Mater.* **2018**, *30*, 1800613.
15 Dai, S.; Zhao, F.; Zhang, Q.; Lau, T.-K.; Li, T.; Liu, K.; Ling, Q.; Wang, C.; Lu, X.; You, W.; Zhan, X. Fused nonacyclic electron acceptors for efficient polymer solar cells. *J. Am. Chem. Soc.* **2017**, *139*, 1336−1343.
16 Dai, S.; Li, T.; Wang, W.; Xiao, Y.; Lau, T.; Li, Z.; Liu, K.; Lu, X.; Zhan, X. Enhancing the performance of polymer solar cells via core engineering of NIR-absorbing electron acceptors. *Adv. Mater.* **2018**, *30*, 1706571.
17 Liao, X.; Yao, Z.; Gao, K.; Shi, X.; Zuo, L.; Zhu, Z.; Chen, L.; Liu, F.; Chen, Y.; Jen, A. K. -Y. Mapping nonfullerene acceptors with a novel wide bandgap polymer for high performance polymer solar cells. *Adv. Energy Mater.* **2018**, *8*, 1801214.
18 Shi, X.; Liao, X.; Gao, K.; Zuo, L.; Chen, J.; Zhao, J.; Liu, F.; Chen, Y.; Jen, A. K. -Y. An electron acceptor with broad visible-NIR absorption and unique solid state packing for as-cast high performance binary organic solar cells. *Adv. Funct. Mater.* **2018**, *28*, 1802324.
19 Zhang, J.; Xu, G.; Tao, F.; Zeng, G.; Zhang, M.; Yang, Y. (Michael); Li, Y.; Li, Y. Highly efficient semitransparent organic solar cells with color rendering index approaching 100. *Adv. Mater.* **2019**, *31*, 1807159.
20 Chang, Y.; Zhu, X.; Zhu, L.; Wang, Y.; Yang, C.; Gu, X.; Zhang, Y.; Zhang, J.; Lu, K.; Sun, X.; Wei, Z. Regioregular narrow bandgap copolymer with strong aggregation ability for high-performance semitransparent photovoltaics. *Nano Energy* **2021**, *86*, 106098.
21 Li, Y.; Lin, J. D.; Liu, X.; Qu, Y.; Wu, F. P.; Liu, F.; Jiang, Z. Q.; Forrest, S. R. Near-infrared ternary tandem solar cells. *Adv. Mater.* **2018**, *30*, 1804416.
22 Liu, Y.; Cheng, P.; Li, T.; Wang, R.; Li, Y.; Chang, S. Y.; Zhu, Y.; Cheng, H. W.; Wei, K. H.; Zhan, X.; Sun, B.; Yang, Y. Unraveling sunlight by transparent organic semiconductors toward photovoltaic and photosynthesis. *ACS Nano* **2019**, *13*, 1071−1077.
23 Liu, S.; Li, H.; Wu, X.; Chen, D.; Zhang, L.; Meng, X.; Tan, L.; Hu, X.; Chen, Y. Pseudo-planar heterojunction organic photovoltaics with optimized light utilization for printable solar windows. *Adv. Mater.* **2022**, *34*, 2201604.
24 Wang, J.; Zhang, J.; Zhou, Y.; Liu, H.; Xue, Q.; Li, X.; Chueh, C.-C.; Yip, H.-L.; Zhu, Z.; Jen, A. K. Y. Highly efficient all-inorganic perovskite solar cells with suppressed non-radiative recombination by a lewis base. *Nat. Commun.* **2020**, *11*, 177.
25 Li, C.; Wang, H.; Wang, F.; Li, T.; Xu, M.; Wang, H.; Wang, Z.; Zhan, X.; Hu, W.; Shen, L. Ultrafast and broadband photodetectors based on a perovskite/organic bulk heterojunction for large-dynamic-range imaging. *Light Sci. Appl.* **2020**, *9*, 31.
26 Li, C.; Jiang, G.; Yu, J.; Ji, W.; Liu, L.; Zhang, P.; Du, J.; Zhan, C.; Wang, J.; Tang, B. Z. Fluorination enhances NIR-II emission and photothermal conversion efficiency of phototheranostic agents for imaging-guided cancer therapy. *Adv. Mater.* **2023**, *35*, 2208229.
27 Liao, X.; Xie, W.; Han, Z.; Cui, Y.; Xia, X.; Shi, X.; Yao, Z.; Xu, X.; Lu, X.; Chen, Y. NIR photodetectors with highly efficient detectivity enabled by 2D fluorinated dithienopicenocarbazole-based ultra-narrow bandgap acceptors. *Adv. Funct. Mater.* **2022**, *32*, 2204255.
28 Dai, S.; Zhou, J.; Lau, T.-K.; Rech, J. J.; Liu, K.; Xue, P.; Xie, Z.; Lu, X.; You, W.; Zhan, X. Effects of fluorination position on fused-ring electron acceptors. *Small Struct.* **2020**, *1*, 2000006.
29 Yao, Z.; Cao, X.; Bi, X.; He, T.; Li, Y.; Jia, X.; Liang, H.; Guo, Y.; Long, G.; Kan, B.; Li, C.; Wan, X.; Chen, Y. Complete peripheral fluorination of the small-molecule acceptor in organic solar cells yields efficiency over 19%. *Angew. Chem. Int. Ed.* **2023**, *135*, e202312630.
30 Aldrich, T. J.; Matta, M.; Zhu, W.; Swick, S. M.; Stern, C. L.; Schatz, G. C.; Facchetti, A.; Melkonyan, F. S.; Marks, T. J. Fluorination effects on indacenodithienothiophene acceptor packing and electronic structure, end-group redistribution, and solar cell photovoltaic response. *J. Am. Chem. Soc.* **2019**, *141*, 3274−3287.
31 Wang, J.; Chen, H.; Li, C.; Lin, Y.; Yang, Y.; Ma, Z.; Lu, Y. Synergistic direct and indirect central unit fluoridation of non-fullerene acceptor enables high-efficiency organic solar cells. *Chem. Eng. J.* **2023**, *477*, 147091.
32 Liu, K.; Jiang, Y.; Ran, G.; Liu, F.; Zhang, W.; Zhu, X. 19.7% efficiency binary organic solar cells achieved by selective core fluorination of nonfullerene electron acceptors. *Joule* **2024**, 8, 835−851.
33 Xie, M.; Shi, Y.; Zhu, L.; Zhang, J.; Cheng, Q.; Zhang, H.; Yan, Y.; Zhu, M.; Zhou, H.; Lu, K.; Wei, Z. Selective halogenation of central and end-units of nonfullerene acceptors enables enhanced molecular packing and photovoltaic performance. *Energy Environ. Sci.* **2023**, *16*, 3543−3551.
34 Meng, D.; Zheng, R.; Zhao, Y.; Zhang, E.; Dou, L.; Yang, Y. Near-infrared materials: the turning point of organic photovoltaics. *Adv. Mater.* **2022**, *34*, 2107330.
35 Li, Z.; Wang, X.; Zheng, N.; Saparbaev, A.; Zhang, J.; Xiao, C.; Lei, S.; Zheng, X.; Zhang, M.; Li, Y.; Xiao B.; Yang, R. Over 17% efficiency all-small-molecule organic solar cells based on an organic molecular donor employing a 2D side chain symmetry breaking strategy. *Energy. Environ. Sci.* **2022**, *15*, 4338−4348.
36 Wei, W.; Zhou, X.; Pang, S.; Zhou, J.; Yuan, X.; Li, J.; Chen, Y.; Pan, L.; Xie, Z.; Wu, H.; Huang, F.; Cao, Y.; Duan, C. A-D-A′-D-A type nonfused ring electron acceptors for efficient organic solar cells via synergistic molecular packing and orientation control. *Aggregate* **2024**, *5*, e488.
37 Miao, W.; Liu, Y.; Wu, Y.; Liang, J.; Xiong, J.; Hu, T.; He, Y.; Chen, L.; Shan, J.; Wang, X.; Yang, R. Energy disorder suppression, charge transport channel establishment by integrating four-arm donor molecule for high-performance organic solar cells. *Adv. Funct. Mater.* **2025**, *35*, 2501143.
38 Chen, J.; Wu, Y.; Chen, L.; Liao, Y.; Zhu, Y.; Saparbaev, A.; Wan, M.; Wu, J.; Li, Y.; Xiang, H.; Saidkulova, A.; Wang, X.; Yang, R. "1+2" alloy-like strategy: restricting molecular diffusion enables highly thermally-stable and efficient organic solar cells. *Adv. Funct. Mater.* **2025**, *35*, e08397.
39 Tao, J.; Yang, K.; Qiu, D.; Wang, C.; Zhang, H.; Lv, M.; Zhang, J.; Lu, K.; Wei, Z. Synergetic optimizing quinoxaline and selenophene substitution in non-fullerene acceptors for efficient organic solar cells. *Nano Energy* **2024**, *125*, 109540.
40 Zou, Y.; Chen, H.; Bi, X.; Xu, X.; Wang, H.; Lin, M.; Ma, Z.; Zhang, M.; Li, C.; Wan, X.; Long, G.; Zhaoyang, Y.; Chen, Y. Peripheral halogenation engineering controls molecular stacking to enable highly efficient organic solar cells. *Energy Environ. Sci.* **2022**, *15*, 3519−3533.
41 Cui, Y.; Yao, H.; Zhang, J.; Zhang, T.; Wang, Y.; Hong, L.; Xian, K.; Xu, B.; Zhang, S.; Peng, J.; Wei, Z.; Gao, F.; Hou, J. Over 16% efficiency organic photovoltaic cells enabled by a chlorinated acceptor with Increased open-circuit voltages. *Nat. Commun.* **2019**, *10*, 2515.
42 Zong, G.; Li, M.; Jin, K.; Xu, Z.; Zhang, L.; Ma, N.; Wang, J.; Wang, G.-W.; Xiao, Z.; Ding, L. Low-bandgap small molecule acceptors with asymmetric side chains. *Mater. Chem. Front.* **2022**, *6*, 1858−1864.
43 Lu, T.; Chen, F. Multiwfn: a multifunctional wavefunction analyzer. *J. Comput. Chem.* **2012**, *33*, 580−592.

https://doi.org/10.1007/s10118-026-3655-0

44 Lu, T. A comprehensive electron wavefunction analysis toolbox for chemists, multiwfn. *J. Chem. Phys.* **2024**, *161*, 082503.
45 Cheng, F.; Lai, S.; Zhang, Y.; Xue, L.; Xia, X.; Zhu, P.; Lu, X.; Liao, X.; Chen, Y. Random terpolymer based on simple siloxane-functionalized thiophene unit enabling high-performance non-fullerene organic solar cells. *Chinese J. Polym. Sci.* **2024**, *42*, 311−321.
46 Zhang, L.; Mao, H.; Huang, L.; Hu, L.; Wang, X.; Tan, L.; Chen, Y. Achieving improved stability and minimal non-radiative recombination loss for over 18% binary organic photovoltaics via versatile interfacial regulation strategy. *Sci. China Chem.* **2022**, *6*, 1623−1633.
47 An, K.; Zhong, W.; Peng, F.; Deng, W.; Shang, Y.; Quan, H.; Qiu, H.; Wang, C.; Liu, F.; Wu, H.; Li, N.; Huang, F.; Ying, L. Mastering morphology of non-fullerene acceptors towards long-term stable organic solar cells. *Nat. Commun.* **2023**, *14*, 2688.
48 Wang, J.; Wang, Y.; Bi, P.; Chen, Z.; Qiao, J.; Li, J.; Wang, W.; Zheng, Z.; Zhang, S.; Hao, X.; Hou, J. Binary organic solar cells with 19.2% efficiency enabled by solid additive. *Adv. Mater.* **2023**, *35*, 2301583.
49 Zhang, H. L.; Wang, Y. T.; Sun, W. J.; Zhang, Y.; Zhang, B. Y.; Ding, Y. T.; Zhang, Z. Q.; Meng, L.; Huang, K.; Ma, W. Integrated omnidirectional design of non-volatile solid additive enables binary organic solar cells with efficiency exceeding 19.5%. *Angew. Chem. Int. Ed.* **2025**, *64*, e202417643.
50 Cui, Y.; Zhu, P.; Hu, H.; Xia, X.; Lu, X.; Yu, S.; Tempeld, H.; Eichel, R.; Liao, X.; Chen, Y. Impact of electrostatic interaction on non-radiative recombination energy losses in organic solar cells based on asymmetric acceptors. *Angew. Chem. Int. Ed.* **2023**, *62*, e202304931.
51 Ma, L.; Yao, H.; Wang, J.; Xu, Y.; Gao, M.; Zu, Y.; Cui, Y.; Zhang, S.; Ye, L.; Hou, J. Impact of electrostatic interaction on bulk morphology in efficient donor-acceptor photovoltaic blends. *Angew. Chem. Int. Ed.* **2021**, *60*, 15988−15994.